

**Effect of alloying elements on microstructural evolution in oxygen content controlled
Ti-29Nb-13Ta-4.6Zr (wt. %) alloys for biomedical applications during aging**

T. Homma ^{a,*}, A. Arafah ^a, D. Haley ^b, M. Nakai ^c, M. Niinomi ^d, M. P. Moody ^b

^a Department of Mechanical Engineering, Nagaoka University of Technology, Nagaoka 940-2188, Japan

^b Department of Materials, University of Oxford, Parks Road, Oxford OX1 3PH, United Kingdom

^c Department of Mechanical Engineering, Kindai University, Higashiosaka City 577-8502, Japan

^d Institute for Materials Research, Tohoku University, Sendai 980-8577, Japan, Graduate School of Engineering, Osaka University, Osaka 565-0871, Japan, Graduate School of Science and Technology, Meijyo University, Nagoya 468-8502, Japan, and Institute of Materials and Systems for Sustainability, Nagoya University, Nagoya 464-8603, Japan

Abstract

The effects of alloying elements in Ti-29Nb-13Ta-4.6Zr (wt. %) (TNTZ) alloys with low Young's modulus for biomedical applications on microstructural evolution during aging, in particular, at an aging temperature of 400 °C have been determined. The peak hardness is obtained by co-precipitation of α and ω phases. O addition stabilizes ω phases; as a result, formation of ω is enhanced with increasing the O content as an alloying element, resulting in prevention of the growth of the α phases due to soft impingement. Because of the stress caused by the ω to α transformation, the α phase often contains defects within its internal structure. Although Zr is known to be a neutral element within Ti, here we show that Zr acts as weak β stabilizer. At the β/α interface, Zr enrichment appears to be due to a solute drag mechanism. In addition, a slight increase in Zr composition in the β/ω interface has also been

* Corresponding author. Tel.: +81 258 47 9760; Fax: +81 258 47 9770.
E-mail address: thomma@mech.nagaokaut.ac.jp (T. Homma)

detected using atom probe. Dispersion of ω phases and segregation of Zr to the β/α interface lead to fine α phase precipitation, resulting in an increase in the hardness of the O-added TNTZ alloys.

Keywords: Ti alloy, biomaterial, age hardening, omega phase, transmission electron microscopy, atom probe

1. Introduction

Biomaterials have widely been investigated and developed for the application of artificial implant materials. The possible applications are stents, replacement implants and so on [1]. Originally, stainless steels were utilized for total joint replacement arthroplasty, and these materials were replaced by Co-Cr-Mo (VitalliumTM) and Ti-6Al-4V Extra Low Interstitial (Ti64 ELI) alloys [2]. The requirements for the usage of biomaterials in medical devices include: high strength, biocompatibility, wear resistance, corrosion resistance, fracture toughness, low elastic modulus and osseointegration [1]. In particular, Ti alloys are attractive as biomaterials since they meet these demands due to their excellent strength, corrosion resistance and osseointegration [3]. However, many Ti alloys, for example the Ti64 ELI alloy, possess high Young's moduli, which lead to undesirable stress shielding. Hence, the development of Ti alloys with low Young's moduli is critical.

At the relatively early stage of the development of Ti alloys with low Young's modulus for biomedical applications, Ahmed et al. developed a new low modulus and biocompatible Ti-35.3Nb-5.1Ta-7.1Zr (wt.%) alloy — so called TNZT [2,4]. This alloy was designed through the incorporation of biocompatible metallic elements such as Ti, Nb, Ta and Zr. Morinaga et al. started by designing new β -type Ti alloys using a “DV- $X\alpha$ cluster method” [5,6]. They succeeded in preparing high strength Ti alloys by controlling the deformation

mechanism. Kuroda et al. utilized this alloy design technique to reduce the elastic moduli of new Ti alloys, and then developed a Ti-29Nb-13Ta-4.6Zr (wt. %) alloy — so called TNTZ that possesses a low Young's modulus and mechanical properties sufficient for implant materials [7].

The TNTZ alloy here not only exhibits a low Young's modulus, but also a high strength due to prior plastic deformation, for example rolling or forging [8,9], and subsequent age-hardening treatments [8,10]. Moreover, oxygen (O) additions can usually increase the strength of Ti alloys even in commercially pure Ti [11]. The remarkable increase in strength that can be achieved by O addition is likely due to solid solution strengthening [e.g., 12]. However, this also degrades elongation and deformation performance. Nakai et al. have previously applied this idea for the strengthening of TNTZ alloys, and found that the age-hardening response is well improved by increasing the O content [13]. Nevertheless, while O addition in the TNTZ alloy is beneficial with respect to strengthening, Young's moduli of the O-added TNTZ alloys are significantly increased, even in the as-quenched (AQ) state.

Pure Ti exhibits polymorphic transformations, and the transformation temperature is 882 °C above which body-centered cubic (bcc) structure is stable, and below which hexagonal close packed structure (hcp) is stable [11]. The former and the latter are called as β and α phases, respectively. It is known that Al and O act as α stabilizers, while Nb, Ta and Fe are known as β stabilizers [11]; Zr, Hf and Sn are categorized as neutral elements, and hence in principle they do not affect structural stabilization. Thus, the TNTZ alloy is a β -type Ti alloy with added Nb and Ta. Although Zr is known to be a neutral element, it has been demonstrated that by controlling the amount of Zr concentration, grain size can be decreased in the case of rolled α -type Ti-Zr alloys [14]. In addition, a grain refinement effect of Zr in α Ti was recently reported [15]. Zr segregates near α grain boundaries, resulting in a decrease

in the grain size due to a solute drag mechanism. The effect of Zr addition on the microstructural evolution in TNTZ has indeed never been explained.

Thus, in this study, we have prepared TNTZ alloys with differing O concentrations, and then applied age-hardening treatments at 300 or 400 °C. The microstructural evolution during aging has been observed using transmission electron microscopy (TEM). The effect of additional elements on the microstructural evolution has then been identified.

2. Experimental procedures

Three alloys were investigated in this study. The alloy compositions measured by inductively coupled plasma mass spectrometry are listed in [Table 1](#). Hereafter, the alloys are denoted as 0.1, 0.2 and 0.4 alloys, depending on the O content. The alloys were melted using a levitation melting method, and the materials were then swaged. The samples were provided from Institute for Materials Research in Tohoku University. Bars of length ~100 mm and diameter 20 mm were cut and encapsulated in a quartz tube under an Ar atmosphere. The samples were then solution heat treated at 790, 800 and 810 °C for 1 h for the 0.1, 0.2 and 0.4 alloys, respectively. These solution-treatment (ST) temperatures were determined to be above 50 °C of their β transus temperatures, respectively. After the ST, the samples were then quenched into ice water. Hereafter these are referred to as AQ samples. Just after the ST, the samples were then aged at 300 or 400 °C for various times (see [Fig. 1](#)), and the samples were again quenched into ice water.

Vickers hardness (H_V) measurements were utilized so as to evaluate the age-hardening curves for each alloy. The conditions of the H_V measurement were undertaken at a 10 kgf load and 10 s holding time. During the measurements, 12 points were evaluated, and after

removing the maximum and minimum hardness, the average hardness was calculated from the remaining 10 data points.

Thin foils for TEM observations were prepared using a Gatan PIPS ion mill, cooled by liquid nitrogen. TEM observations were then carried out using a JEOL JEM-2100F TEM operated at 200 kV. High angle annular dark field scanning TEM (HAADF-STEM) observations were carried out using its scanning transmission electron microscopy (STEM) mode. Elemental maps were acquired by site-specific examination of precipitation phases using a JEOL JED-2300T energy dispersive X-ray (EDX) spectrometer. Point analysis of α , β and the β/α interface was also performed using the EDX spectrometer. The measurement was conducted by observing HAADF-STEM images, and the used spot size was 0.7 nm. In particular, the composition profile across the β/α interface was carefully measured.

Atom probe analysis was performed on the 0.4 wt. % O content samples aged at 300 °C. Samples were prepared by a standard focused ion beam lift-out [16], using a Zeiss N-Vision 40 Dual-beam SEM/FIB, with an initial accelerating voltage of 30 kV, finally reduced to 5 kV to limit implantation damage. Atom probe tomography (APT) data was acquired on a Cameca LEAP 5000 HR, with a fitted reflectron. The experiment was performed in laser mode, using a laser energy of 30 pJ, at a set temperature of 40 K and a pulse repetition rate of 200 kHz. In total, two datasets were acquired from these specimens of 25 M and 6.2 M, respectively. Some initial implantation damage was detected in the 6.2 M ion dataset, and the data cropped such that the global Ga content was $\ll 0.1$ at. %. The global concentration is given in Table 2. O in the OH₂ peak was found to be 0.01 at. % of the total dataset and is not considered to alter the reported O composition considerably. This peak is thus ignored for the APT analysis, as this is otherwise ambiguous with residual chamber water vapour. The two compositions shown in Table 2 were largely in agreement, with small variations in Nb, Zr, Fe

and O levels, which may arise from either spatial inhomogeneity or alternately from experimental variability.

3. Results

Figure 1 shows the age-hardening curves of the 0.1, 0.2 and 0.4 alloys aged at 400 °C. In the AQ state, the hardness of the 0.4 alloy is much higher than that of the 0.1 and 0.2 alloys; the difference between the hardness of 0.4 and 0.1 alloys is approximately 100. In the underaged condition, the hardness of the 0.4 alloy is higher, and all the alloys show a gradual increase in the hardness with aging time. At peak hardness, the maximum Hv values of 356 at 432.0×10^3 s, 343 at 604.8×10^3 s and 325 at 777.6×10^3 s are acquired in the 0.4, 0.2 and 0.1 alloys, respectively. It should be noted that the time for reaching the peak hardness is greatly reduced with increasing O content, indicating that O addition promotes the precipitation kinetics. After peak hardness, all the hardness decreases due to their overaged states.

Bright field (BF) images and the corresponding selected-area electron diffraction (SAED) patterns of the AQ, 24 h-aged, peak-aged (PA) and overaged (OA, 950.4×10^3 s) samples are presented in Fig. 2. In all the alloys, there is no precipitation in their AQ states; nevertheless, the respective hardness measurements reveal a large difference between them. Since there are no additional spots in the SAED patterns, we can conclude that the increase in the hardness in the 0.4 and 0.2 alloys are due to solid solution strengthening by dispersing O atoms within the β matrix.

In the underaged condition (24 h aging), precipitation of α phases can be confirmed in both the 0.1 and 0.2 alloys, though it does not precipitate in the 0.4 alloy. The width of the α phases is larger with decreasing O content. In addition, there are reflections from ω phases only in the 0.1 alloy, as indicated by white arrows in Fig. 2.

At the PA condition, a number of precipitates appear in all alloys. It is found that the number density of α phases seems to increase with aging time, as shown in Fig. 3. Diffraction spots shown in Fig. 2 can be interpreted when the Bergers orientation relationship is considered [17]; i.e., $\{011\}_{\beta} // (0001)_{\alpha}$ and $[11\bar{1}]_{\beta} // [\bar{1}210]_{\alpha}$ [e.g. 18]. Other diffraction spots can be interpreted as double diffraction [19]. Since α and ω phases coexist in the PA conditions, their contribution to the SAED patterns should be understood, and hence high resolution transmission electron microscope (HRTEM) images are acquired from each phase. The results and the fast Fourier transformed (FFT) patterns are given in Fig. 4. If the α phase is placed during the observation, the spots appear, e.g., at $1/2 (112)_{\beta}$. It is interesting to note that the spots occasionally accompany streaks as shown in the key diagram given in Fig. 2. If we compare HRTEM images of α phases, for example, between 0.2 and 0.4 alloys, there are fringe patterns within the α phase in the 0.4 alloy. The streaks appeared in the FFT pattern in the 0.4 alloy are perpendicular to the fringe patterns observed in the real space. Since we expect α phases impinge on ω phases during aging particularly in the 0.4 alloys, it can be interpreted that the streaks are related to the deformation of α .

A quantitative evaluation of the size of α has been performed by selecting a hundred of the α phase in each alloy, and the results are given in Table 3. The measurements are obtained by considering the α phase to be lath shaped, and the length and width are measured from HAADF-STEM images such as Fig. 3. Moreover, spots surrounding the spots relating to the α phase at the $1/3$ and $2/3 (112)_{\beta}$ positions are due to isothermal ω precipitation [20], indicating that ω phase coprecipitates with α at the PA conditions (Fig. 4). Figure 3 shows the morphology of the ω phases in both the 0.1 and 0.4 alloys, as observed in the dark field (DF) images, each taken using one of the four representative spots of ω . It seems that the

morphology of ω may be lath-shaped and their length along their longitudinal axes decreases with increasing O content. From the DF images given in Fig. 3, area fractions (AFs) of the ω phases are roughly evaluated. The AFs in 0.1, 0.2 and 0.4 alloys are 14, 33 and 34%, respectively. Thus, the AFs seem to be increased as the O content increases at the PA conditions.

A closer look at the interaction between the α and ω phases given in Fig. 3 demonstrates that they independently precipitate and may impede each other, leading to pinning of the α precipitations by the presence of the ω phases due probably to “soft impingement” [21]. As a result, the size of the α phase is decreased as indicated in the BF and HAADF-STEM images (see also Fig. 2).

Figure 5 details the partitioning behavior of each element to either the β or α phases, as determined by measuring the composition of alloying elements in β or α by EDX spot analysis. The measurements were carried out from 10 different areas of β and α phases, and the results were averaged out so as to calculate partitioning coefficient. The partitioning coefficient is defined as $\kappa_i = X_{i\beta}/X_{i\alpha}$, where $X_{i\beta}$ and $X_{i\alpha}$ denote composition of element, i , in β and α , respectively. This technique is often utilized, for example, in the field of Ni-based superalloys [22]. Regardless of the aging condition and O content, Ta, Nb and Zr are partitioned into the β phase, while Ti is partitioned into the α phase. These results coincide well with reported stabilizing effects [11], except for Zr. Indeed, Zr behaves like weak β stabilizer. Moreover, the partitioning behavior of O is odd as indicated by black arrows, although it is usually known as α stabilizer; the behavior here is likely to be β stabilizing. We then assume that the results of EDX analysis cannot avoid composition measurement from ω phases so that they cannot be visualized using BF and HAADF-STEM images. It is

therefore possible that the contribution of composition from ω was involved in the results of O composition measurements.

In order to understand the partitioning behavior of additional elements only in the ω phase, the time-temperature-transformation (TTT) diagram of a TNTZ alloy reported by Hao et al. was utilized [23]; the O content here is close to that in the 0.2 alloy in their investigated TNTZ alloy. At 400 °C, such as for the alloy used in this research, β , α and ω phases appear to form. On the other hand, when the aging temperature is decreased to 300 °C, then from this TTT data, it is expected that only the ω phase forms in the β matrix. We then measured an age-hardening curve at 300 °C, and the result was shown in Fig. 6. Here, we only deal with the 0.4 alloy so that the effect of O addition on partitioning behavior is estimated to be obvious compared to the other 0.1 and 0.2 alloys. The hardness of the 0.4 alloy is very high, and the maximum hardness is comparable to that obtained in the 0.4 alloy aged at 400 °C. Even under AQ conditions, the Hv value exceeds 300.

We then observed the microstructures of the PA and OA (1.2×10^4 s) conditions by TEM, with the results given in Fig. 7. When the incident beam was inclined parallel to $[\bar{1}10]_\beta$, spots at the $1/3$ and $2/3$ $(112)_\beta$ positions appear, indicating the formation of isothermal ω , as estimated from a TTT diagram [23]. As the aging time increases such as OA conditions, then double diffraction at $1/3$ and $2/3$ $(110)_\beta$ positions is intensified due to coarsening of the ω phase. The morphology of the ω phase seems to be lath shaped, and the size increases in the OA sample. The number density is significantly high, even in the PA sample. We then again measure the partitioning coefficients between β and ω phases in the PA and OA samples of the 0.4 alloy aged at 300 °C using EDX spot analysis. Here we define the partitioning coefficient as $\kappa_2 = X_{i\beta}/X_{i\omega}$, where $X_{i\beta}$ and $X_{i\omega}$ denote composition of element, i , in β and ω ,

respectively. The results are shown in Fig. 8. As expected, O tends to partition into ω phase. The partitioning behavior of other elements is very similar to that obtained at 400 °C aging.

In order to confirm the portioning behavior, APT analysis was performed for the PA samples of the 0.4 alloy aged at 300 °C as shown in Fig. 9. To delineate the precipitates from the matrix and determine their respective chemistries, within the first dataset an initial iso-threshold of 79 at. % Ti (voxel size $3 \times 3 \times 1.5$ nm) was selected to visually separate the precipitate phase, as this appeared to have the best discrimination. However, to obtain a more objective delineation between the two phases, and to ensure accurate selection of the interior and exterior regions of the dataset, a logistic function was fitted to the measured composition profile.

$$Ti(x) = K \left(\frac{1}{1 + e^{-\lambda(x-x_0)}} \right) - 0.5 + y_0$$

From the curve fit the midpoint of the transition zone, y_0 , was determined, a new isosurface calculated using the y_0 value, and the fit repeated until the result minimized the interface width ($1/\lambda$), yielding 73.1 at. % Ti, shown in Fig. 10. For the second dataset, the narrowest transition zone was found at a Ti concentration of 72.9 at. %. A fit based upon the transition width, $1/\lambda$, was used to select the > 0.95 relative zone (> 0.95 for the centered, unit scaled transfer function, $\lambda = 1$, $x_0 = 0$, $y_0 = 0.5$) of the transfer function, which corresponds to $x = \pm 2.94/\lambda$. This ensures that the composition reported is minimally affected by transition region of the transfer function. Here the upper and lower bounds corresponded to a Ti composition of $> 84.6\%$ (precipitate) and < 61.56 at. % (matrix) in the first case. In the second dataset, the upper and lower limits for separating matrix and precipitate were $Ti < 58.9$ at. % and $Ti > 87.0$ at. %. The compositions of this data are given in Table 4.

O was found to mainly occur in the form of ZrO and NbO ions. Whilst some O was found at $m/c = 16$, this was determined to be O^+ , as the alternate peaks for Ti^{3+} were not

sufficiently intense, although the total amplitude at mass 16 is low. Thus, peak overlaps were not a concern for measuring O concentration within the dataset. From this, we report measured O concentrations for the precipitates and matrix to be 2.0 and 0.79 at. %, respectively for the first dataset, while 1.56 and 0.64 at. %, respectively, for the second. Thus, there is a clear partitioning to the precipitate phase in both cases, with a partitioning coefficient of 0.39 and 0.41, respectively, in good agreement with the EDX data.

Notably, whilst the majority of other species in the material did not show any noticeable segregation to either phase, Zr was found to be enriched in the transition zone from the matrix to precipitates. A similar result is visible in existing APT data of TNTZ alloys [24], but was not discussed. In the results shown in Fig. 11, Zr segregation up to a peak concentration of 5 and 4 at. % (dataset 1 and 2) was identified, and it appears that the variability is non-symmetric in the reported proximity histogram, with the segregation appearing at the matrix side of the computed interface.

Composition profiles measured across β/α interfaces in 0.1, 0.2 and 0.4 alloys of PA samples at 400 °C are obtained by the EDX spot analysis. The results are summarized in Figs. 12 and 13. Here, the positions of the β/α interface are indicated by gray dotted lines which are parallel to the vertical axis. As expected from Fig. 5, both Nb and Ta are partitioned into the β phase, while Ti is enriched in the α phase. Nevertheless, while Zr is usually expected to be a neutral element, enrichment of Zr near the interface is confirmed, as shown in Fig. 13. As a reference, average compositions of α and β phases in all the alloys are summarized in Table 5. Nb, Ta and Zr are enriched in β phase. There are no large composition differences, irrespective of type of the used alloys.

4. Discussion

Observed hardness increases are related to the precipitation of α and ω phases in all the investigated alloys aged at 400 °C. The morphology of the α phase most likely is of a thin lath shape, while that of ω phase is also likely to be lath shaped. The addition of O promotes solid solution strengthening in the AQ state. In addition, the O addition diminishes size of the α phase at the peak hardness. As indicated in Fig. 3, we found that the volume fraction of the ω phase seems to be increased with the O content; here, we assumed that the area fraction of the ω phase is proportional to its volume fraction. This may imply that the addition of O may influence formation of the ω phase in the underaged condition. There may be interaction between the ω and α phases as estimated from soft impingement, specifically that the growth of the α phases is restricted by it, leading to fine α precipitations. Furthermore, in the 0.1 alloy aged for 24 h, formation of ω and α phases are fast, indicating that the kinetics of the precipitates are suppressed by O addition. We found that O is mainly partitioned into the ω phase, and nucleation of ω may further be enhanced in the 0.2 and 0.4 alloys. This effect may retard the kinetics of ω and α phase formation, and as such their nucleus size could be very small compared with those in the 0.1 alloy. Consequently, the sizes of α and ω phases may be large in the 0.1 alloy aged for 24 h. In general, both the α and ω phases enhance the strength of β -type Ti alloys [25], and hence we can conclude that the peak hardness is obtained due to concurrent precipitations of the α and ω phases.

It should be emphasized that the size of α phase is diminished by O addition at the peak hardness. The size of the α phase was evaluated using HAADF-STEM images. Here, we measured length and width of the lath-shaped α phase. By calculating the aspect ratio (length/width), we estimated the effect of α phases on strength, as given in Table 3. Thus, the O addition reduces the size of the α phase (Fig. 3). Based on fundamental precipitation

strengthening theory [e.g. 26], the fine and dense distribution of the strengthening phase such as α gives rise to high strength.

As shown in the SAED patterns of PA and OA samples in Fig. 2, streaks appear near the spots relating to α phases ($1/2 (112)_\beta$). The origin of the streaks can be detected by HRTEM observations, and the results are shown in Fig. 4. It seems that the streaks arise from defects, such as stacking faults (SFs, gray arrows in an HRTEM image in Fig. 4), occurring in the α phase. Nishiyama et al. reported that when SFs appear, for instance in a Cu-12.3Au (wt.%) alloy, streaks appear in the corresponding SAED patterns [28]. The SFs are related to formation of β' martensite. Since α' martensite, whose structure is a hexagonal close-packed (hcp), appears in Ti alloys [11,28], a similar interpretation should be acceptable. In the PA state, α and ω phases coexist (Figs. 2 and 3). The ω phase may apply a stress to adjacent α phases with soft impingement, resulting in the local deformation of α phases. This deformation leads to the appearance of SFs as observed in the HRTEM images shown in Fig. 4 (gray arrows). The presence of these SFs causes streaks in the corresponding SAED patterns (Fig. 2). Indeed, similar results are also reported by Knowles and Smith in Ti-Mn systems which possess hcp martensites [29]. By definition, the α phase with the streaks should be called as α' martensite [30], but the α' martensite basically appears as an athermal transformation product during quenching [12]. Thus, there are at least two types of α phases in this study, i.e. (1) with and (2) without SFs (Fig. 4). The former is therefore called as “deformed α phases” in this study.

The partitioning behavior of alloying elements in TNTZ is investigated, and the results are shown in Figs. 5 and 8. Ta, Nb and Ti have a common text-book behavior [11], while Zr and O do not: Zr is weak β stabilizer, while O is ω stabilizer—O stabilizes not only ω but also α . κ_1 and κ_2 increase as with aging time. This indicates that the compositions of Nb, Ta and

Zr in β phase and Ti in α phase also increase with aging time. General compositions in the α and β phases are given in Table 5. A similar tendency of O partitioning can be estimated even in ω phase aged at 300 °C. Our APT results demonstrate that O is indeed preferentially partitioned into the ω phase (Table 4). Thus, any enhancement in age hardenability of investigated-TNTZ alloys is strongly related to O addition and its effect on the formation of the isothermal ω phase. Moreover, we also found that a slight increase in Zr composition in the β/ω interface as well. This may affect the size of the ω phase.

As depicted in Fig. 12, composition profiles near β/α interface shows round shapes regarding Ti, Nb and Ta. This indicates that the growth of α phase is a diffusion-controlled process [21]. Nb and Ta are β stabilizer [11], and thus, they are involved in β phase. As a result of rejecting those elements from α , Ti is enriched in the α phase. Most interesting results in Fig. 13 are the segregation of Zr near the β/α interface. As reported previously [15], Zr tends to be on the trailing sides near the interface during the growth of α , although the composition is slightly low. If the Zr segregation near all the β/α interface occurs, the low concentration of Zr is reasonable. During growth of α phase due to aging, Zr remains inside of the α phase since Zr is slow diffuser in α Ti [15,31]. This may cause a solute drag effect which retards the growth of the α phase, leading to fine α size distribution. Eventually, the fine α , as shown in Figs. 2 and 3, enhance the strength of TNTZ alloys (Fig. 1). This indicates that Zr may stabilize β in the AQ state and remained in β matrix. During nucleation of α phase, Zr may be involved in α phases. When the growth of the α phase starts, Zr segregates near the α/β interface. This behavior is in contrast to typical reports of Zr, acting as a neutral element [11].

5. Conclusions

We have investigated the effects of alloying elements on microstructural evolution in several TNTZ alloys, each having a controlled O content, so as to enhance the age-hardening response at 400 °C. The following conclusions were obtained. In the AQ states, the hardness increment is related to solid solution hardening by O. Peak hardness is obtained by the co-precipitation of α and ω phases when the samples are aged at 400 °C. O addition reduces the size of α precipitates. Based on the results of measurement of partitioning behavior and APT analysis, it is found that the O addition stabilizes ω phases with segregation of Zr around them. Since O addition stabilizes ω phase, formation of ω may be enhanced with increasing the O content as an alloying element, resulting in the prevention of growth of the α phase, due to soft impingement. Because of the stress caused by ω to α , the α phase sometimes contains defects in its internal structure. Although Zr is typically reported to be a neutral element in Ti alloys, it is observed to act as weak β stabilizer. At the β/α interface, Zr enrichment appears. Dispersion of ω phases and segregation of Zr to the β/α interface due to a solute drag mechanism leads to fine α phase precipitation when aged at 400 °C, resulting in an increase in hardness in the O-added TNTZ alloys. Based on EDX spot analysis perpendicular to the β/α interface, it is also found that growth of α phase is a diffusion-controlled process.

Acknowledgments — This work was in part supported by Grant-in-Aid for Scientific Research (C), 15K07100, 2015, Japan and the Inter-University Cooperative Research Program of the Institute for Materials Research, Tohoku University (Proposal No. 14K0027 & 15K0035). TH is also grateful for financial support from Union Tool Co., Japan. DH and MM acknowledge the support of the EPSRC under the HEmS Programme Grant

EP/L014742/1. We acknowledge Mr. H. Takano of Nagaoka University of Technology, Japan for his experimental support.

References

- [1] M. Geetha, A.K. Singh, R. Asokamani, A.K. Gogia, *Prog. Mater. Sci.* 54 (2009) 397-425.
- [2] M. Long, H.J. Rack, *Biomaterials* 19 (1998) 1621-1639.
- [3] T. Hanawa, *Sci. Technol. Adv. Mater.* 12 (2012) 064102.
- [4] T. Ahmed, M. Long, J. Silvestri, H.J. Rack, *Proceedings in Eighth World Conference on Titanium*, P.A. Blenkinsop, W.J. Evans and H.M. Flower, Eds., The Institute of Materials, Birmingham, (1996) 1760-1767.
- [5] H. Adachi, T. Mukoyama, J. Kawai, Eds, *Hartree-Fock-Slater method for materials science*, Springer, Berlin, 2006.
- [6] M. Morinaga, M. Kato, T. Kamimura, M. Fukumoto, I. Harada, K. Kubo, *Titanium'92, Science and Technology*, F.H. Froes, I. Caplan, Eds, *Proc. 7th Int. Conf. on Titanium*, San Diego, CA, (1992) 276-283.
- [7] D. Kuroda, M. Niinomi, M. Morinaga, Y. Kato, T. Yashiro, *Mater. Sci. Eng. A* 243 (1998) 244-249.
- [8] M. Niinomi, T. Hattori, K. Morikawa, T. Kasuga, A. Szuki, H. Fukui, S. Niwa, *Mater. Trans.* 43 (2002) 2970-2977.
- [9] T. Akahori, M. Niinomi, H. Fukui, A. Suzuki, *Mater. Trans.* 45 (2004) 1540-1548.
- [10] M. Ikeda, S. Komatsu, I. Sowa, M. Niinomi, *Met. Mater. Trans. A* 33A (2002) 487-493.
- [11] C. Leyens, M. Peters, Eds, *Titanium and titanium alloys—fundamentals and applications*, WILEY-VCH, Oxford, 2003.
- [12] R. Boyer, G. Welsch, E.W. Collings, *Materials Properties Handbook: titanium alloys*, 4th ed., ASM International, Materials Park, OH, 1994.
- [13] M. Nakai, M. Niinomi, T. Akahori, H. Tsutsumi, M. Ogawa, *Mater. Trans.* 50 (2009) 2716-2720.

- [14] N. Sakaguchi, M. Niinomi, T. Akahori, H. Toda, J. Japan Inst. Met. 70 (2006) 89-95.
- [15] T. Homma, Y. Matayoshi, R. Voskoboynikov, Phil. Mag. Lett. 95 (2015) 564-573.
- [16] K. Thompson, D. Lawrence, D.J. Larson, J.D. Olson, T.F. Kelly, B. Gorman, Ultramicroscopy 107 (2007) 131-139.
- [17] W.G. Burgers, Physica 1 (1934) 561-586.
- [18] H.P. Ng, P. Nandwana, A. Devaraj, M. Semblanet, S. Nag, P.N.H. Nakashima, S. Meher, C.J. Bettles, M.A. Gibson, H.L. Fraser, B.C. Muddle, R. Nanerjee, Acta Mater. 84 (2015) 457-471.
- [19] D.B. Williams, C.B. Carter, Transmission electron microscopy, Diffraction II, Plenum, New York, 1996.
- [20] E. Suckedai, Titanium and titanium alloys—fundamentals and applications, C. Leyens, M. Peters, Eds, WILEY-VCH, Oxford, 2003.
- [21] J.W. Christian, the theory of transformations in metals and alloys, part 1, 3rd ed., Pergamon, Oxford, 2002.
- [22] O.H. Kriege, J.M. Baris, Trans. ASM 62 (1969) 195-200.
- [23] Y.L. Hao, M. Niinomi, D. Kuroda, K. Fukunaga, Y.L. Zhou, R. Yang, A. Suzuki, Metal. Mater. Trans. A 34A (2003) 1007-1012.
- [24] M. Niinomi, M. Nakai, M. Hendrickson, P. Nandwana, T. Alam, D. Choudhuri, R. Banerjee, Scripta Mater. 123 (2016) 144-148.
- [25] K. Narita, M. Niinomi, M. Nakai, T. Akahori, K. Oribe, T. Tamura, S. Kozuka, S. Sato, J. Japan Int. Metals 72 (2008) 674-678.
- [26] A. Kelly, R.B. Nicholson, Prog. Mater. Sci. 10 (1963) 148-391.
- [27] Z. Nishiyama, J. Kakinoki, S. Kajiwarra, J. Phys Soc. Jpn. 20 (1965) 1192-1211.
- [28] J.C. Williams, Titanium science and technology, vol. 3, Plenum, New York, 1973.

- [29] K.M. Knowles, D.A. Smith, *Acta Met.* 29 (1981) 1445-1466.
- [30] Z. Nishiyama, *Martensitic transformation*, M.E. Fine, M. Meshii, C.M. Wayman, Eds, Academic press, New York, 1978.
- [31] R.A. Perez, H. Nakajima, F. Dymont, *Mater. Trans.* 44 (2003) 2-13.

Table 1 Chemical composition of the investigated alloys.

Table 1

Alloy	-	Nb	Ta	Zr	O	Ti
0.1	wt. % (at. %)	29.2 (20.3)	13.0 (4.6)	4.7 (3.3)	0.07 (0.28)	bal.
0.2	wt. % (at. %)	30.6 (21.3)	13.2 (4.7)	4.4 (3.1)	0.19 (0.77)	bal.
0.4	wt. % (at. %)	30.3 (21.1)	13.6 (4.8)	4.4 (3.1)	0.37 (1.49)	bal.

Table 2 Composition of the two analyzed samples, as reported by APT. PA stands for peak aged.

Table 2

Species	300 °C PA	
	Composition (at. %)	Composition (at. %)
Ti	70.3	70.4
Nb	20.6	19.7
Ta	4.3	4.3
Zr	3.4	3.7
O	1.3	1.63
Fe	0.06	0.16
Ga	0.02	0.025

Table 3 Evaluation of size of α phases at the PA conditions. L, W and A denote length, width and aspect ratio, respectively.

Table 3

Alloy	L [nm]	W [nm]	A
0.1	197.8 ± 88.5	25.1 ± 16.2	10.5 ± 5.9
0.2	123.6 ± 54.7	9.0 ± 3.6	14.4 ± 6.0
0.4	110.5 ± 37.9	10.0 ± 4.0	12.2 ± 5.1

Table 4 Compositional analysis of matrix and precipitate regions, with data separated into matrix and precipitate regions, as defined by a logistic curve cut, excluding the transition zone. Quantities are in at. %, and have been background corrected.

Table 4

300 °C PA, Nominal O=0.4	Dataset 1		Dataset 2	
Counts	Matrix	Precipitate	Matrix	Precipitate
Ti	58.4	91.8	59.4	90.4
Nb	31.1	2.94	30.2	3.83
Ta	6.31	1.1	5.58	1.12
Zr	3.35	2.52	3.73	2.64
O	0.65	1.56	0.79	1.97
Fe	0.08	-	0.20	0.04
C	0.02	-	0.03	-
Ga	0.02	-	0.03	-
N	0.02	-	0.04	-
Al	0.02	-	0.03	-

Table 5 Average compositions of α and β phases in the 0.1, 0.2 and 0.4 alloys measured by EDX spot analysis (at. %). The selected-aging time was 604.8×10^3 s (168 h) in all the alloys.

Table 5

Alloy	α phase				β phase			
	Nb	Ta	Zr	Ti	Nb	Ta	Zr	Ti
0.1	10.1 ± 19.0	5.0 ± 2.7	4.5 ± 1.6	bal.	31.2 ± 3.3	4.7 ± 0.4	5.9 ± 0.7	bal.
0.2	11.6 ± 4.0	2.0 ± 0.6	4.5 ± 0.5	bal.	32.8 ± 2.4	4.3 ± 1.6	5.3 ± 0.9	bal.
0.4	13.4 ± 7.9	2.7 ± 1.2	4.3 ± 0.7	bal.	28.3 ± 6.8	4.7 ± 0.8	5.7 ± 1.6	bal.

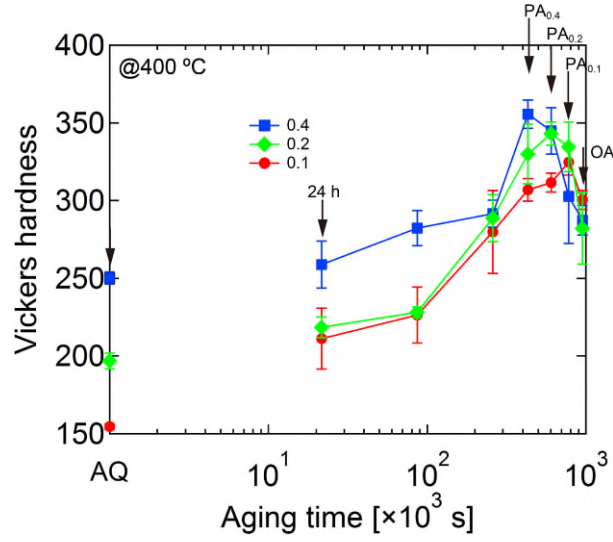


Figure 1

Figure 1 Age-hardening curves of the 0.1, 0.2 and 0.4 alloys measured at 400 °C. PA and OA denote peak-aged and overaged states, respectively. TEM observations were performed at the aging times indicated by black arrows. Times at PA_{0.4}, PA_{0.2} and PA_{0.1} are 432.0×10^3 , 604.8×10^3 and 777.6×10^3 s, respectively.

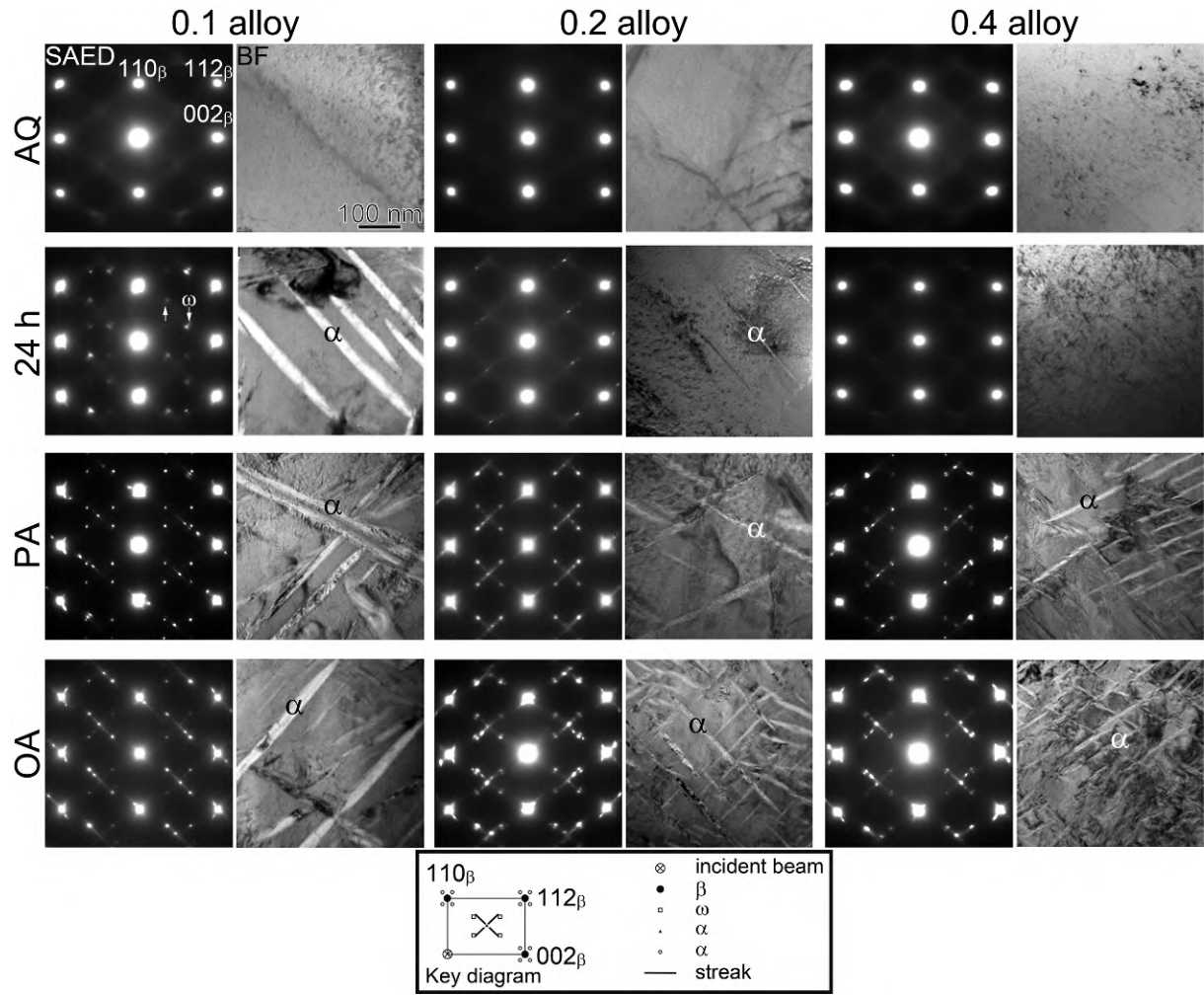


Figure 2

Figure 2 BF images and corresponding SAED patterns of 0.1, 0.2 and 0.4 alloys ($\mathbf{B} // [\bar{1}10]_{\beta}$). Observation conditions are AQ, underaged (24 h), PA and OA as shown in [Fig. 1](#). The white arrows show diffracted spots concerning ω phase. A key diagram associated with the SAED patterns are also included.

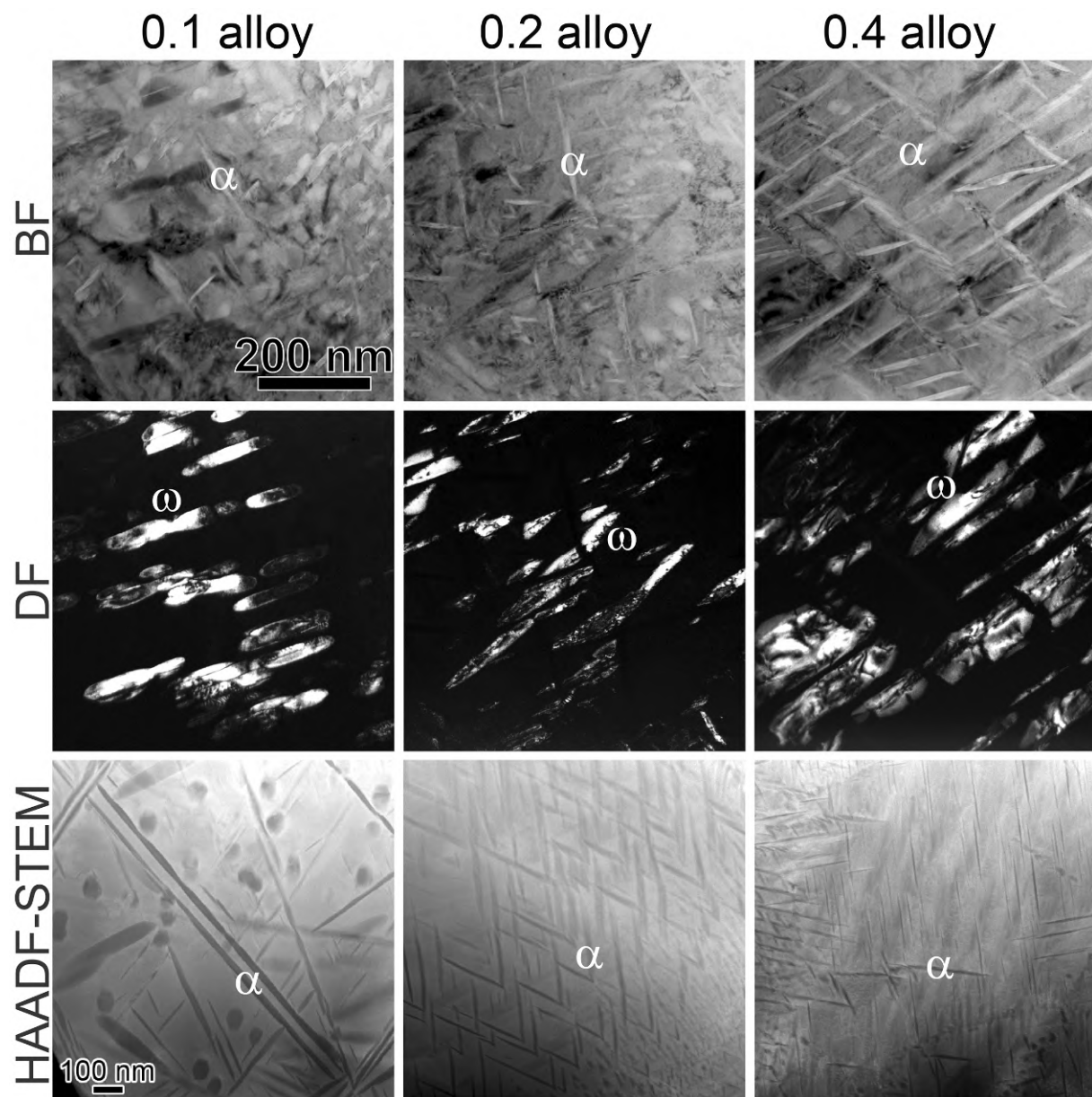


Figure 3

Figure 3 BF and corresponding DF images of the PA conditions of 0.1, 0.2 and 0.4 alloys. For the measurement of size of the α phases, HAADF-STEM images are also observed.

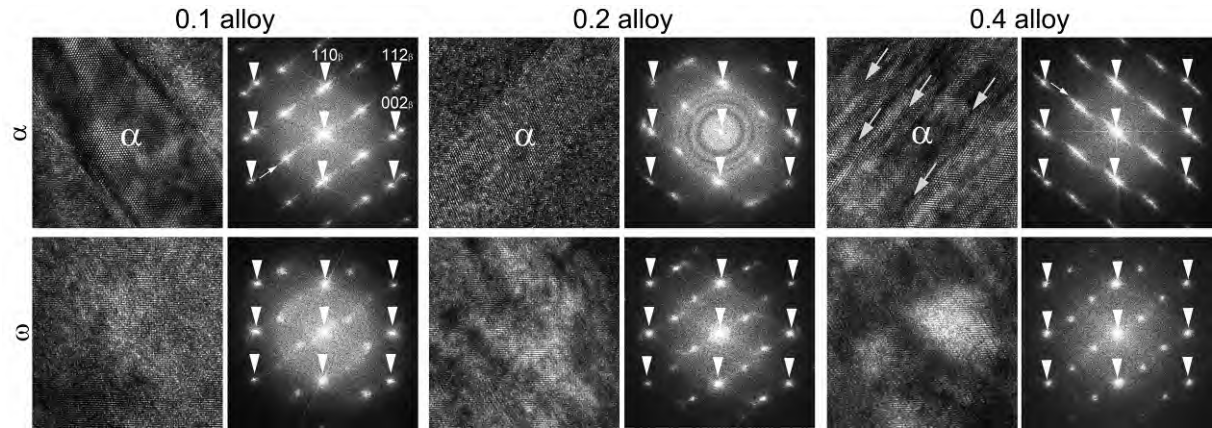


Figure 4

[Figure 4](#) HRTEM images and corresponding FFT patterns of the PA conditions of 0.1, 0.2 and 0.4 alloys ($\mathbf{B} // [\bar{1}10]_{\beta}$). The α and ω phases are detected. The white arrowheads indicate diffracted spots from the β matrix, whilst white arrows show streaks due to deformation of the α phases. Such streaks can often be seen in SAED patterns given in [Fig. 2](#) (see key diagram).

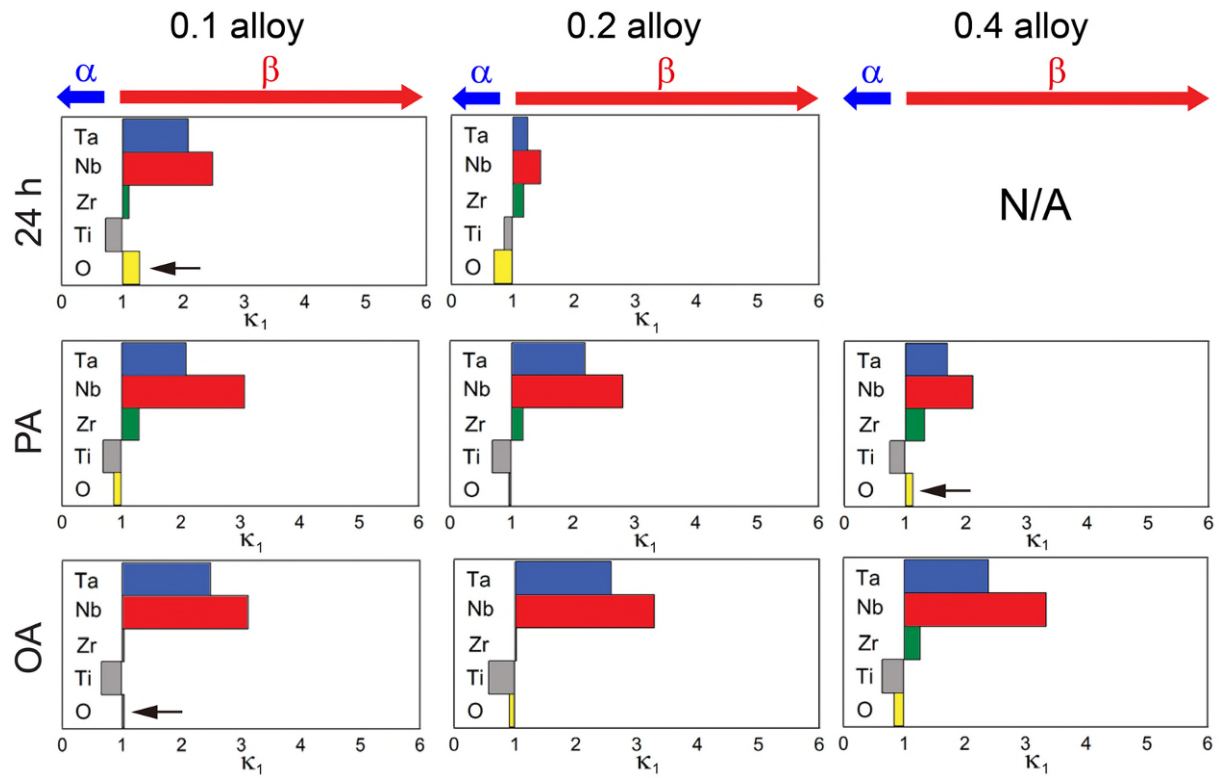


Figure 5

Figure 5 Partitioning behavior of additional elements in the β and α phases at 400 °C. κ_1 denotes a partitioning coefficient. There are no α phases in 0.4 alloy aged for 24 h, see Fig. 2.

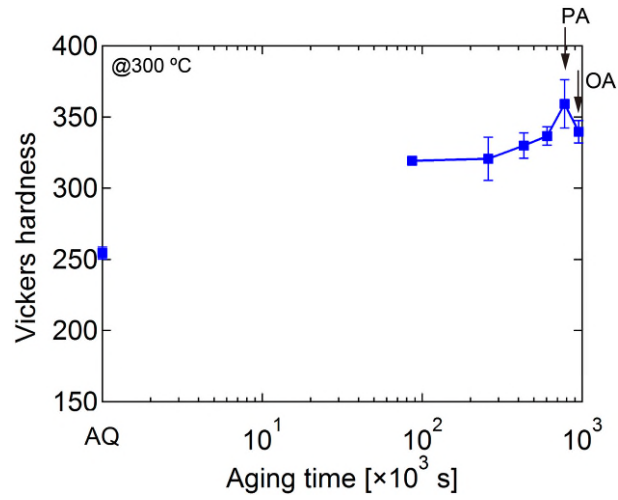


Figure 6

Figure 6 An age-hardening curve of the 0.4 alloy measured at 300 °C. PA and OA denote peak-aged and overaged states, respectively. TEM observations were performed at the aging times indicted by black arrows. Times at PA, and OA are 777.6×10^3 and 1209.6×10^3 s, respectively.

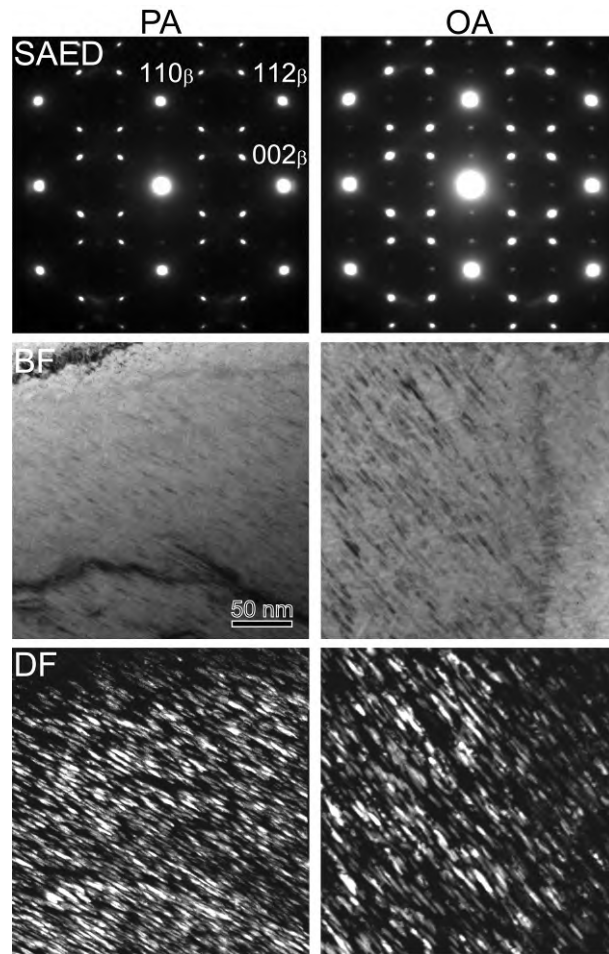


Figure 7

Figure 7 SAED patterns ($\mathbf{B} // [\bar{1}10]_{\beta}$) and BF and corresponding DF images of PA and OA conditions of the 0.4 alloys aged at 300 °C.

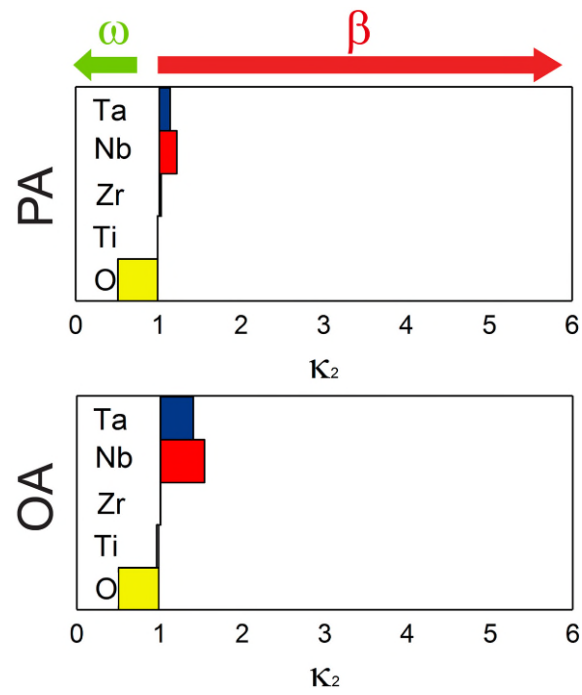


Figure 8

Figure 8 Partitioning behavior of additional elements in the β and ω phases at 300 °C. κ_2 denotes a partitioning coefficient.

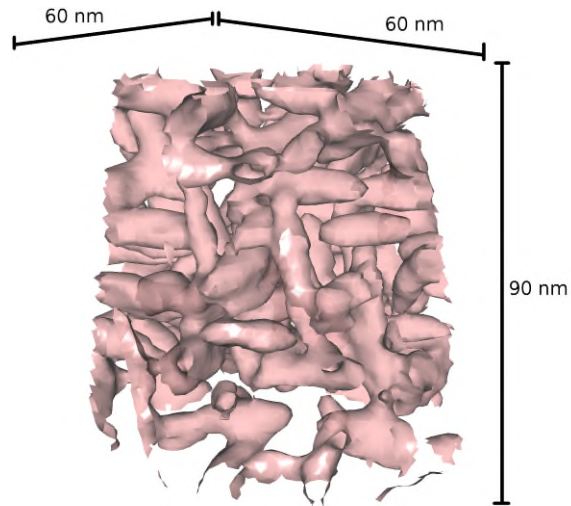


Figure 9

Figure 9 An APT elemental map obtained from the 0.4 alloy aged at 300 °C, acquired using a LEAP 5000 system in laser pulsing mode. The data is shown as a compositional isosurface (Ti = 73.1%), optimized to minimize the interfacial width between the two phases. The precipitates shown in the isosurface are ω phases ([Fig. 7](#)).

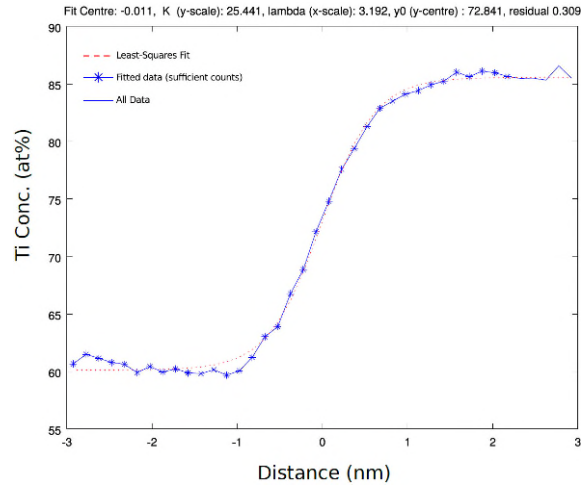


Figure 10

Figure 10 Logistic curve fit to proximity histogram of Ti, using a 73.1 at. % Ti isosurface for the 300 °C PA dataset.

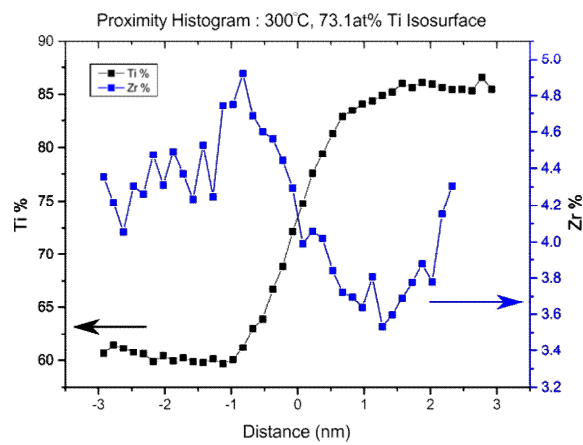


Figure 11

Figure 11 Zr segregation to precipitate interface segregation appears to occur on the Ti lean side of the precipitate/matrix interface.

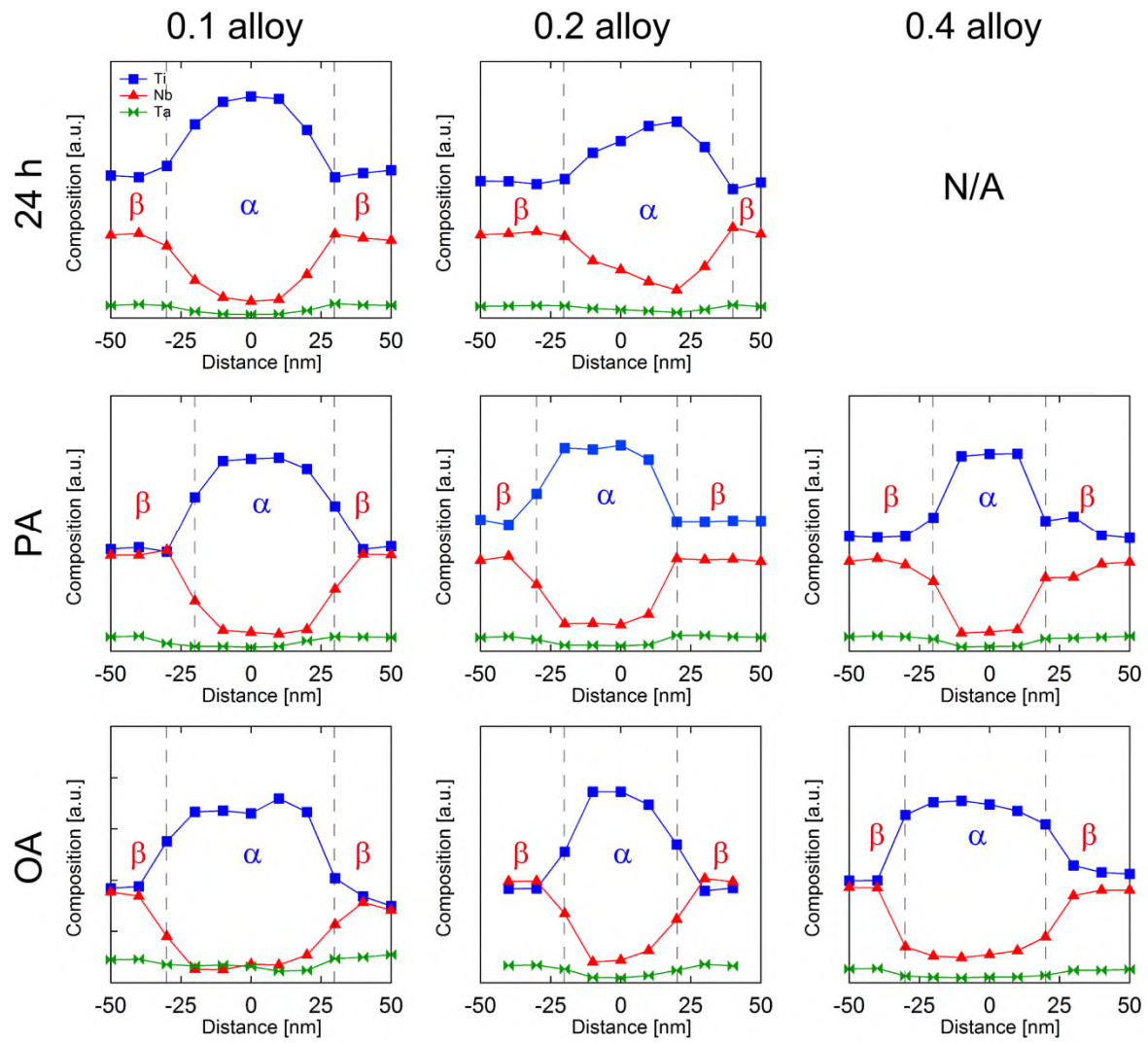


Figure 12

Figure 12 Composition profiles across β/α interfaces. The profile is plotted as a function of distance. The gray dotted lines depict positions of the interface.

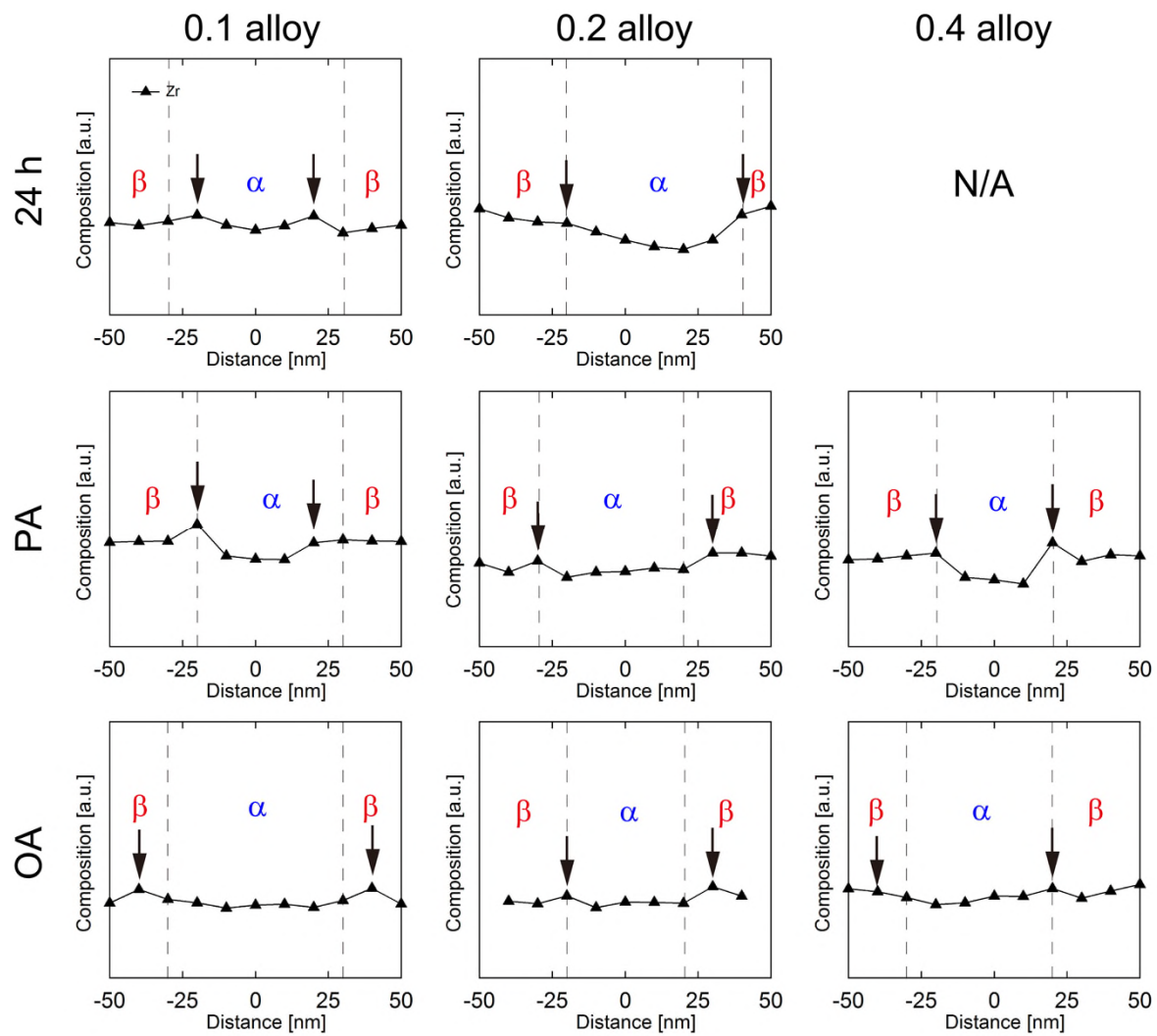


Figure 13

Figure 13 Zr composition profiles across β/α interfaces. The profile is plotted as a function of distance. The gray dotted lines depict positions of the interface, and the arrows indicate appearance of Zr enrichment near the interface.